JAEA-Data/Code
2021-002
DOI:10.11484/jaea-data-code-2021-002

A Numerical Simulation Study of the Desaturation and Oxygen Infusion into the Sedimentary Rock around the Tunnel in the Horonobe Underground Research Laboratory

Kazuya MIYAKAWA, Kazuhei AOYAGI, Toshifumi AKAKI and Hajime YAMAMOTO

Horonobe Underground Research Department
Horonobe Underground Research Center
Sector of Nuclear Fuel, Decommissioning and Waste Management Technology Development

May 2021

Japan Atomic Energy Agency

日本原子力研究開発機構

JAEA-Data/Code

国立研究開発法人日本原子力研究開発機構　研究連携成果展開部　研究成果管理課
〒 319-1195　茨城県那珂郡東海村大字白方 2 番地 4
電話 029-282-6387, Fax 029-282-5920, E-mail:ird-support@jaea.go.jp

JAEA-Data/Code 2021-002

A Numerical Simulation Study of the Desaturation and Oxygen Infusion into the Sedimentary Rock around the Tunnel in the Horonobe Underground Research Laboratory

Kazuya MIYAKAWA, Kazuhei AOYAGI, Toshifumi AKAKI* and Hajime YAMAMOTO*

Horonobe Underground Research Department
Horonobe Underground Research Center
Sector of Nuclear Fuel, Decommissioning and Waste Management Technology Development
Japan Atomic Energy Agency
Horonobe-cho, Teshio-gun, Hokkaido

(Received January 20, 2021)

Investigations employing numerical simulation have been conducted to study the mechanisms of desaturation and oxygen infusion into sedimentary formations. By mimicking the conditions of the Horonobe underground research laboratory, numerical simulations aided geoscientific investigation of the effects of dissolved gas content and rock permeability on the desaturation (Miyakawa et al., 2019[1)]) and mechanisms of oxygen intrusion into the host rock (Miyakawa et al., 2021[2)]). These simulations calculated multi-phase flow, including flows of groundwater and exsolved gas, and conducted sensitivity analysis changing the dissolved gas content, rock permeability, and humidity at the gallery wall. Only the most important results from these simulations have been reported previously, because of publishers' space limitations. Hence, in order to provide basic data for understanding the mechanisms of desaturation and oxygen infusion into rock, all data for 27 output parameters (e.g., advective fluxes of heat, gas, and water, diffusive fluxes of water, CH_4, CO_2, O_2, and N_2, saturation degree, water pressure, and mass fraction of each component) over a modeling period of 100 years are presented here.

Keywords: Desaturation, Oxygen Intrusion, Dissolved Gas, EDZ, Geological Disposal

---

* Taisei Corporation

1) Miyakawa, K., Aoyagi, K., Sasamoto, H., Akaki, T., Yamamoto, H., The effect of dissolved gas on rock desaturation in artificial openings in geological formations, Extended abstract of YSRM2019 and REIF2019, Ginowan, Japan, 2019, 6p.

2) Miyakawa, K., Aoyagi, K., Akaki, T., Yamamoto, H., Numerical simulation of oxygen infusion into desaturation resulting from artificial openings in sedimentary formations, 15th Japan Symposium on Rock Mechanics, Osaka, Japan, 2021, 6p.

JAEA-Data/Code 2021-002

幌延深地層研究センター地下施設における坑道周辺の堆積岩を対象とした不飽和領域の形成及び岩盤中への酸素の侵入要因に関する数値解析データ

日本原子力研究開発機構 核燃料・バックエンド研究開発部門
幌延深地層研究センター 深地層研究部

宮川　和也，青柳　和平，赤木　俊文*，山本　肇*

(2021 年 1 月 20 日受理)

これまでに，堆積岩を対象とした不飽和領域の形成及び岩盤中への酸素の侵入要因の検討を目的とした数値解析を実施してきた。Miyakawa et al. (2019)[1)]では，堆積岩地域の例として，幌延深地層研究センターの地下施設を模擬し，これらの解析結果の一部をまとめ，飽和度変化及び不飽和領域の広がりに対する溶存ガス濃度及び岩盤の透水性の及ぼす影響について議論している。Miyakawa et al. (2021)[2)]でも同様に解析結果の一部をまとめ，坑道内の酸素の岩盤中への侵入挙動に対する溶存ガス濃度，岩盤の透水性及び坑道内の湿度の影響について議論している。これらの報告では，テーマを絞った議論のため，一部の解析結果のみしか公開されていない。本報告書は，不飽和領域の形成や岩盤中への酸素の侵入挙動及び坑道の埋戻し後の不飽和領域の消長を考察する上で参考となる基礎データを公開することを目的として，上記の 2 件の検討で使用したデータを含めた全ての解析結果をデータ集として取りまとめたものである。

幌延深地層研究センター：〒098-3224　北海道天塩郡幌延町字北進 432-2
* 大成建設株式会社

1) Miyakawa, K., Aoyagi, K., Sasamoto, H., Akaki, T., Yamamoto, H., The effect of dissolved gas on rock desaturation in artificial openings in geological formations, Extended abstract of YSRM2019 and REIF2019, Ginowan, Japan, 2019, 6p.

2) Miyakawa, K., Aoyagi, K., Akaki, T., Yamamoto, H., Numerical simulation of oxygen infusion into desaturation resulting from artificial openings in sedimentary formations, 15th Japan Symposium on Rock Mechanics, Osaka, Japan, 2021, 6p.

Contents

目次

List of Figures

List of Tables

This is a blank page.

1. Introduction

Geological repository construction inevitably involves drainage of large volumes of groundwater from cracks and pores in surrounding rock, desaturating the rock around the galleries. Desaturation affects the hydraulic properties of rocks, increasing gas mobility relative to groundwater and leading to air infusion into the rocks. Such desaturation is confined more or less to the excavation damaged zone (EDZ) in a claystone formation of very low permeability[1)], which indicates that permeability sensitively controls desaturation. The EDZ is a zone associated with irreversible deformation involving the creation and propagation of fractures in which hydromechanical and geochemical modifications induce significant changes in both flow and transport properties[2)]. The oxidation of the host rock—which is summarized in the Features, Events, and Processes Catalogue for Argillaceous Media (FEPCAT) project by the Organisation for Economic Co-operation and Development/Nuclear Energy Agency (OECD/NEA)—is relevant to the field of excavation, and is connected to EDZ[3)]. During the operation of a repository, transient oxidizing conditions will be encountered because of oxygen in the air. The transient conditions will persist following the repository's closure, and can greatly affect the redox potential and pH. Consequences include increasing solubility of radionuclides and corrosion of the inner steel overpack. Further effects can include mineralogical changes in the host rock, especially pyrite-bearing formations. For Opalinus and Boom clays, oxidation of pyrite in the host rock induced by ventilation of the repository during the operational phase is well understood, and constraints based on oxygen diffusion rates through desaturation in EDZ fractures are likely to provide at least upper bounds on the extent of host rock oxidation[4), 5)].

Construction of the Horonobe underground research laboratory (HURL) commenced in November 2005. The facility is situated in pyrite-bearing sedimentary rocks of the Neogene Koetoi and Wakkanai formations (Fig. 1). The horizontal gallery, at 350 m depth, was completed in June 2014. Humidity in the gallery ranges from 50%–60% in winter to 90%–100% in summer[6)]. Groundwater in these formations contains significant amounts of dissolved CH_4 and CO_2[7)]. These gases emanate from the HURL's gallery walls[8)], and occupy the headspaces of boreholes drilled in the EDZ[9)]. A numerical sensitivity analysis showed that the dissolved gas content affects both the degree of desaturation and its spatial extent, whereas rock permeability affects only the latter[10)]. The results showed that large amounts of dissolved gas enhance the spatial extent of desaturation beyond the EDZ.

Oxidizing conditions did not exist in the HURL's EDZ, which was lined with 0.2-m-thick concrete. This was attributed to the suppression of air intrusion by the release of dissolved gas from groundwater as the pressure decreased, and its subsequent accumulation in fractures[9)]. However, in-situ physico-chemical observations found that, without a shotcrete lining, oxidation and dry areas reached about 0.1 m from the gallery wall[6)]. Miyakawa et al. (2021)[11)] investigated the mechanism of O_2 intrusion into the rock through numerical multiphase flow simulations considering the advection and diffusion of groundwater and gases, where the simulation considered only Darcy's and Henry's laws, and neglected chemical reactions related to the oxidation of pyrite. Dissolved gas and rock permeability had almost

identical effects on O_2 infusion into the rock. High humidity maintained the saturation in the EDZ, leading to limited O_2 intrusion because of very low diffusivity in the solution phase. In contrast, decreasing humidity around relatively low-permeability rock led to extensive accumulation of O_2 in the EDZ, even with a relatively large amount of dissolved gas. In the HURL, shotcrete attenuates O_2 concentration and maintains 100% humidity at the boundary of the gallery wall, which inhibits O_2 infusion.

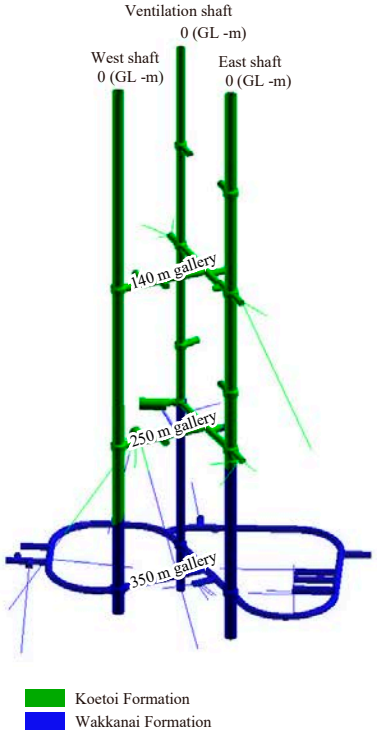

Fig. 1 Layout of the Horonobe URL and surrounding geology
(partly modified from Miyakawa and Okumura (2018)[12])

Only the most important results from these numerical simulations by Miyakawa et al. (2019)[10] and Miyakawa et al. (2020)[11] were published for reasons of space. Hence, in order to provide basic data for understanding the mechanisms of desaturation and oxygen infusion into the rock, all data for 27 output parameters (e.g., advective fluxes of heat, gas, and water, diffusive fluxes of water, CH_4, CO_2, O_2, and N_2, saturation degree, water pressure, and mass fraction of each component) from numerical simulations over a 100-year modeling period are presented here.

The role of each author is as follows: Dr. K. Miyakawa, the first author, planned this study, summarized the results, and wrote the manuscript. Dr. K. Aoyagi, the second author, assisted the planning. Mr. T. Akaki and Dr. H. Yamamoto, respectively the third and the last authors, conducted the numerical calculations.

2. Methodology

2.1 Conceptual model and simulation details

The simulation was performed using the TMVOC[13] numerical analysis program, which is a numerical simulator for three-phase, non-isothermal flow in multidimensional heterogeneous porous media. The simulations were applied to groundwater containing O_2, N_2, CO_2, and CH_4, with dissolution and exsolution of these gases being quantified according to Henry's law (i.e., the amount of gas dissolved is proportional to its partial pressure above the liquid).

According to Jung et al. (2018)[14], mass transfer in TMVOC is calculated as

$$\frac{d}{dt}\int_{V_n} M^\kappa dV = \int_{\Gamma_n} F^\kappa \cdot n d\Gamma + \int_{V_n} q^\kappa dV, \qquad (1)$$

where V_n is an arbitrary subdomain of the flow system under study, which is bounded by a closed surface Γ_n. The quantity M represents the mass or energy of component κ (e.g., water, CH_4, CO_2, O_2, and N_2 or energy h). F denotes mass or heat flux, and q denotes sinks and sources. n is a normal vector on the surface element $d\Gamma_n$, pointing inward into V_n. The general form of the mass accumulation term is

$$M^\kappa = n_e \sum_\beta S_\beta \rho_\beta X_\beta^\kappa, \qquad (2)$$

where n_e is porosity, S_β is the saturation degree of phase β (e.g., β = gas or liquid), ρ_β is the density of phase β, and X_β^κ is the molar ratio of component κ in phase β. The heat accumulation term of M^h is calculated using Eq. (3):

$$M^h = (1-n_e)\rho_R C_R T + n_e \sum_\beta S_\beta \rho_\beta u_\beta \qquad (3)$$

where the subscript R denotes the rock, C_R is the specific heat of the rock grains, T is temperature, and u_β is the specific internal energy of phase β. Advective mass flux is a sum of phase fluxes:

$$F_{\text{adv}}^\kappa = \sum_\beta X_\beta^\kappa F_\beta, \qquad (4)$$

where individual phase fluxes are given by a multiphase version of Darcy's law:

$$F_\beta = \rho_\beta v_\beta = -k\frac{k_{r\beta}\rho_\beta}{\mu_\beta}\left(\nabla P_\beta - \rho_\beta g\right). \qquad (5)$$

Here, v_β is the Darcy velocity (volume flux) of phase β, k is absolute permeability, $k_{r\beta}$ is the relative permeability of phase β, μ_β is dynamic viscosity, and

$$P_\beta = P + P_{c\beta} \qquad (6)$$

is the fluid pressure in phase β, which is the sum of the pressure P of the gas phase and the capillary pressure $P_{c\beta}(\leq 0)$. g is the vector of gravitational acceleration. In addition to Darcy flow, mass

transport by diffusive flux is modeled as follows:

$$F^{\kappa}_{\mathrm{diff}} = \sum_{\beta} -n_e \tau_o \tau_\beta \rho_\beta D^{\kappa}_{\beta} \nabla X^{\kappa}_{\beta}, \qquad (7)$$

where D^{κ}_{β} is the molecular diffusion coefficient for component κ in phase β, and $\tau_o\tau_\beta$ is the tortuosity, which includes a factor τ_o dependent on the porous medium and a coefficient τ_β that depends on phase saturation S_β. Heat flux includes conductive, convective, and radiative components:

$$F^{h} = -\lambda \nabla T + \sum_{\beta} h_\beta F_\beta, \qquad (8)$$

where λ is the effective thermal conductivity, and h_β is the specific enthalpy in phase β.

The solubility of each gas component (CH_4, CO_2, O_2, and N_2) is described by Henry's law:

$$P^{\kappa}_{g} = X^{\kappa}_{g} P_{\mathrm{g}} = X^{\kappa}_{l} K^{\kappa}_{H}, \qquad (9)$$

where P^{κ}_{g} is the partial pressure of component κ, and P_g is the total pressure of the gas phase. X^{κ}_{g} and X^{κ}_{l} are the molar ratios of component κ in gas and liquid phase, respectively, and K^{κ}_{H} is the Henry's constant of component κ.

The model is depicted schematically in Fig. 2, and includes a 1-m-thick rock layer extending from the gallery wall through the EDZ (1 m thick) to a distance of 3 km from the center of the 4-m-diameter gallery. The boundary condition at the inside wall of the gallery is fixed at atmospheric conditions (21% O_2, 79% N_2, 100% humidity, 1.013×10^5 Pa). Initially, the modeled region was filled with water, meaning an initial degree of saturation of 1 throughout, with the initial water pressure being hydrostatic pressure. The temperature at each depth was calculated according to a geothermal gradient of 3 °C per 100 m with a surface temperature of 15 °C. The rock layer was divided into two sections: the EDZ and intact rock. Modeling extended for periods of up to 100 years for the base cases and sensitivity analysis, and up to 1000 years for the analysis of recovery after back filling. Relative permeabilities (m^2) for liquid (k_{rl}) and gas (k_{rg}) were calculated with gaseous and liquid phases coexisting in pore spaces according to the Verma model[15] as in equations (10) and (11), respectively.

$$k_{rl} = 2.9(S_l - 0.3)^3, \qquad (10)$$

$$k_{rg} = 1 - 2.1(S_l - 0.3) + (S_l - 0.3)^2, \qquad (11)$$

where S_l is the degree of saturation. Capillary pressure (p_{cap}) was calculated as a function of the degree of saturation[16] as

$$p_{cap} = -2 \times 10^5 \left(S_l^{-2.2} - 1\right)^{0.54}, \qquad (12)$$

where $-1 \times 10^8 < p_{cap} < 0$ (Pa). The specific coefficients used were determined in a boring survey conducted near the HURL[17]. Effective diffusivity (D_e) was calculated from effective porosity (n_e) as

$$D_e = {n_e}^{4/3} \times D, \qquad (13)$$

where D is a representative value of molecular diffusivity: 5×10^{-10} and 1×10^{-5} m^2 s^{-1} for liquid and gaseous phases, respectively.

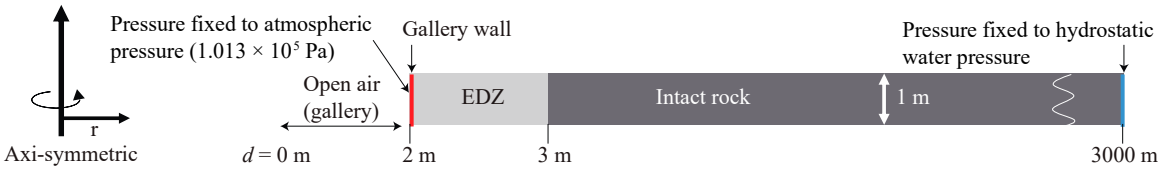

Fig. 2 Conceptual model for the simulation of multiphase flow

At 3000 m from the far gallery wall, the dissolved gas content is fixed to the initial condition[11].

2.2 Base case and sensitivity analysis

Simulations mimicking conditions in each gallery were performed as 'base cases' (Table 1). The conditions of base cases 1, 2, and 3 correspond to those of the 140, 250, and 350 m galleries, respectively, with parameters derived in previous observations and initial water pressure and temperature values applied according to depth.

Table 1 Parameters used for base cases 1–3

	Case 1		Case 2		Case 3	
	EDZ	Intact rock	EDZ	Intact rock	EDZ	Intact rock
Permeability (m^2)	7.5×10^{-14} [18]	1.2×10^{-17} [19]	5.1×10^{-15} [20]	5.2×10^{-17} [19]	1.7×10^{-13} [21]	9.5×10^{-19} [19]
Effective porosity	0.55 [19]		0.50 [19]		0.40 [19]	
Specific storage (m^{-1})	1.4×10^{-4} [18]	1.0×10^{-5} #1	1.0×10^{-5} #2	1.0×10^{-5} #1	3.3×10^{-5} [21]	1.0×10^{-5} #1
EDZ width (m)	1.0 [18]		1.0 [20]		1.0 [22]	
Initial content of dissolved CH_4 (mol L^{-1})	1.9×10^{-2} #3		3.3×10^{-2} #3		4.3×10^{-2} #3	
Initial content of dissolved CO_2 (mol L^{-1})	8.7×10^{-3} #3		6.0×10^{-3} #3		2.0×10^{-2} #3	
Initial water pressure (Pa)	1.37×10^6		2.45×10^6		3.43×10^6	
Temperature (°C)	19.2		22.5		25.5	

#1 According to the deep drilling investigation in the Horonobe area, specific storage shows an almost constant value of 1×10^{-5} m^{-1}, which is below the value 1×10^{-6} m/s for hydraulic conductivity[23].

#2 The specific storage for the EDZ of the 250 m gallery is given as being the same as that of intact rock due to lack of monitoring data.

#3 Saturated concentrations of dissolved gases were calculated using a method proposed by Tamamura et al. (2018)[24] with measurement data reported by Miyakawa et al. (2017)[7].

To investigate the effect of dissolved gas, the initial concentrations of CH_4 and CO_2 were changed for sensitivity analyses in cases 4–12 (Table 2). The permeability study (cases 13–21) compared different values (Table 2), with case 18 having extremely low permeability. For case 12, the temperature was fixed to 50 °C. Cases 22 and 23 had parameters the same as base case 3, although the saturation

degree at the gallery wall was fixed to 60% and 90%, respectively. Cases 24 and 25 had the saturation degree at the gallery wall fixed to 60%, and the other parameters were the same as those in base case 3 except for the effective porosity, which was 0.8 and 0.02, respectively.

Table 2 Parameters changed in cases 4–25[#1]

	Initial content of dissolved gas (mol L^{-1})		Permeability of intact rock (m^2)	Humidity at the boundary of the gallery wall (%)	Corresponding base case	Note
	CH_4	CO_2				
Case 4[#2]	0	0			Case 1	
Case 5[#2]	1.3×10^{-2} [7)]	6.8×10^{-3} [7)]			Case 1	
Case 6[#2]	0	0			Case 2	
Case 7[#2]	1.5×10^{-3} [7)]	4.1×10^{-2} [7)]			Case 2	
Case 8[#2]	0	0			Case 3	
Case 9[#2, #3]	5.0×10^{-4} [7)]	4.9×10^{-2} [7)]			Case 3	
Case 10[#3]	1.5×10^{-2}	1.59×10^{-2}			Case 3	
Case 11[#3]	2.8×10^{-2}	1.63×10^{-2}			Case 3	
Case 12	3.2×10^{-2}	1.1×10^{-2}			Case 3	Temperature was fixed to 50℃.
Case 13[#2]			7.4×10^{-16} [23)]		Case 1	
Case 14[#2]			9.5×10^{-15} [23)]		Case 2	
Case 15[#3]			1.0×10^{-21}		Case 3	
Case 16[#2, #3]			2.6×10^{-16} [23)]		Case 3	
Case 17[#3]			1.0×10^{-15}		Case 3	
Case 18[#2]			9.2×10^{-21}		Case 1	The effective porosity was changed as 0.1, and the EDZ was neglected.
Case 19[#3]			9.5×10^{-21}	50	Case 3	
Case 20[#3]			9.5×10^{-19}	50	Case 3	
Case 21[#3]			9.5×10^{-15}	50	Case 3	
Case 22					Case 3	The saturation degree at the wall was fixed to 60%.
Case 23					Case 3	The saturation degree at the wall was fixed to 90%.
Case 24					Case 3	The effective porosity was changed to 0.8.
Case 25					Case 3	The effective porosity was changed to 0.02.

[#1] Parameters used for these cases are the same as the corresponding base cases except for values in this table.
[#2] Some results from these cases were published in Miyakawa et al. (2019)[10)].
[#3] Some results from these cases were published in Miyakawa et al. (2021)[11)].

2.3 Long-term analysis of recovery from desaturation after drift backfilling

For the long-term analysis of recovery from desaturation mimicking the situation after drift backfilling, output parameters from calculations at 100 years were given as the initial conditions. Table 3 lists the corresponding cases (numbers 26–31) giving the initial conditions for long-term analysis.

Case 26 is the base case. The boundary condition of any flow at the gallery wall was fixed to 0 for cases 26–31. Modeling extended for periods of up to 1000 years.

In investigating the effect of dissolved gas, the initial concentrations of CH_4 and CO_2 were changed for sensitivity analysis in cases 27 and 28. The permeability study compared different values in cases 29 and 30. Case 31 had a higher temperature of 50 °C. The cases were ranked for initial dissolved gas content in the order case 26 > case 27 > case 28. The ordering for permeability was case 29 > case 26 > case 30.

Table 3 List of cases for recovery from desaturation after drift backfilling

	Note
Case 26	Continued from case 3.
Case 27	Continued from case 11.
Case 28	Continued from case 10.
Case 29	Continued from case 17.
Case 30	Continued from case 15.
Case 31	Continued from case 12.

3. Results

This section presents two-dimensional plots (with respect to time) of saturation degree, water pressure, and advective flux of the gas and liquid phases. All the figures have the point for 1 m on the horizontal axis (distance from the wall) corresponding to the boundary between the EDZ and the intact rock. In subsections 3.1, 3.2.1, 3.2.2, 3.2.3, and 3.2.5, only results at 1 day, 10 days, 100 days, 1 year, 10 years, and 50 years are shown. Subsection 3.2.4 shows data for 100 days, 1 year, 10 years, 100 years, 500 years, and 1000 years only.

The Appendix presents all data, including the rest of the output components, as text data. It gives the outputs of 27 components for cases 1–25 at 0 day, 1 day, 10 days, 100 days, half-year, 1 year, 5 years, 10 years, 25 years, 50 years, and 100 years. For cases 26–31, it gives the outputs of 27 components at 0 day, 1 day, 10 days, 100 days, half-year, 1 year, 5 years, 10 years, 100 years, 200 years, 500 years, and 1000 years.

3.1 Base cases

Results for base cases 1–3 are shown in Figs 3–5, respectively. In all cases, the degree of saturation was lowest around the boundary between the EDZ and the intact rock, as shown at the point 1 m from the wall in the figures. This was likely due to the fixed condition of 100% humidity at the gallery wall. The spatial extent of desaturation increased with time in all cases. Water pressure decreased with time in all cases, and drastically decreased in the EDZ within 1 day. Miyakawa et al. (2019 and 2021)[10), 11)] give detailed descriptions and discussion of the desaturation and oxygen infusion.

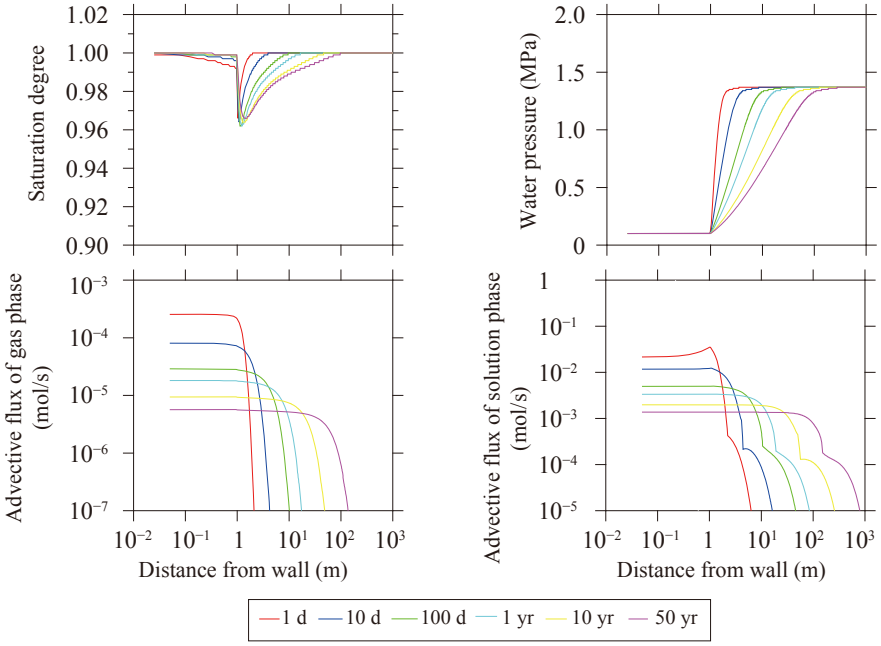

Fig. 3 Simulation results for case 1

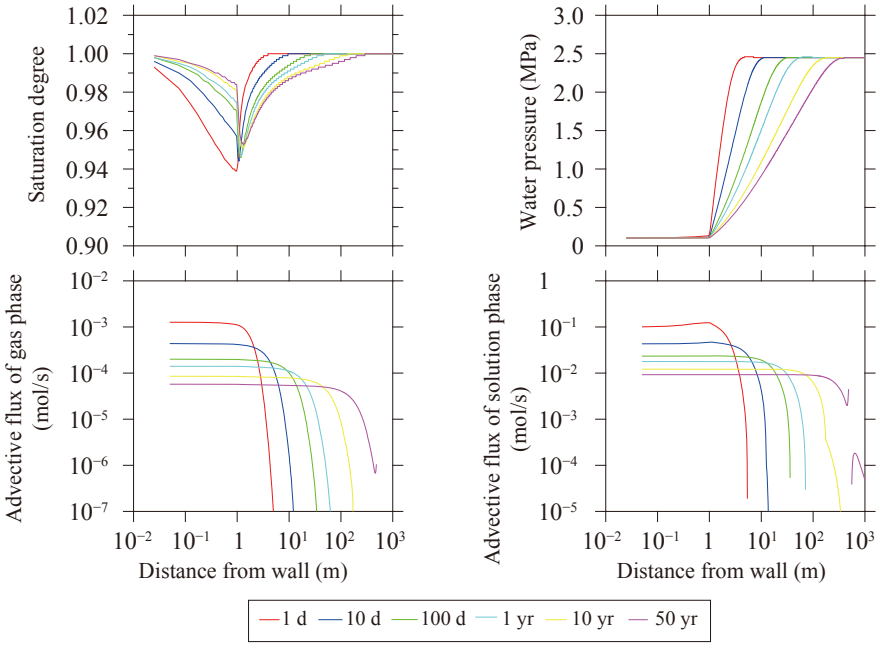

Fig. 4 Simulation results for case 2

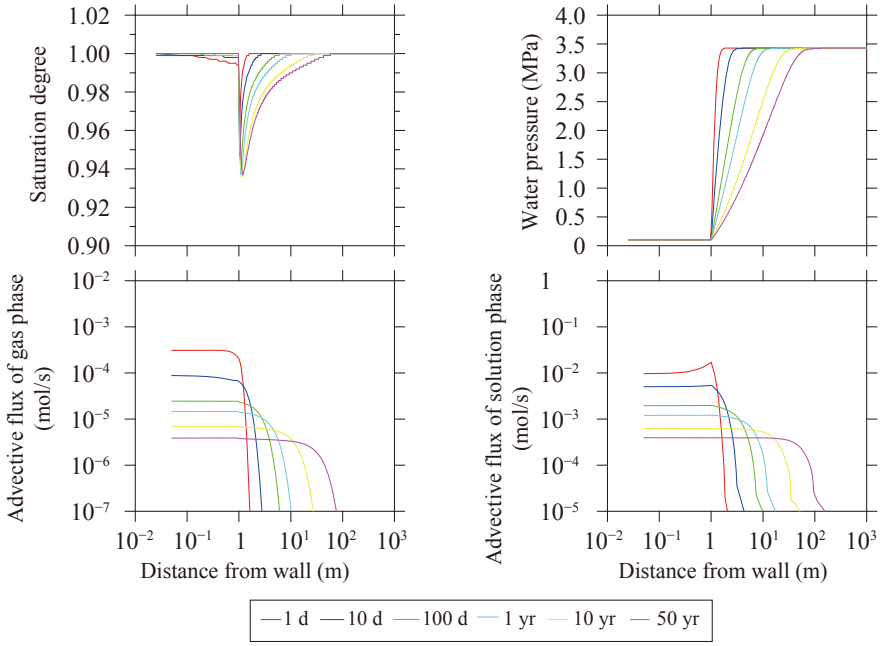

Fig. 5 Simulation results for case 3

3.2 Sensitivity analysis

3.2.1 Effect of initial dissolved gas content

Results for cases 4–12 are shown in Figs 6–14, respectively. The cases without dissolved gases (cases 4, 6, and 8) showed no decrease in the degree of saturation over all distances and times. Water pressure decreased with time in all cases, and drastically decreased in the EDZ within 1 day. Except for case 12, detailed descriptions and discussions of desaturation and oxygen infusion can also be found in Miyakawa et al. (2019 and 2021)[10), 11)].

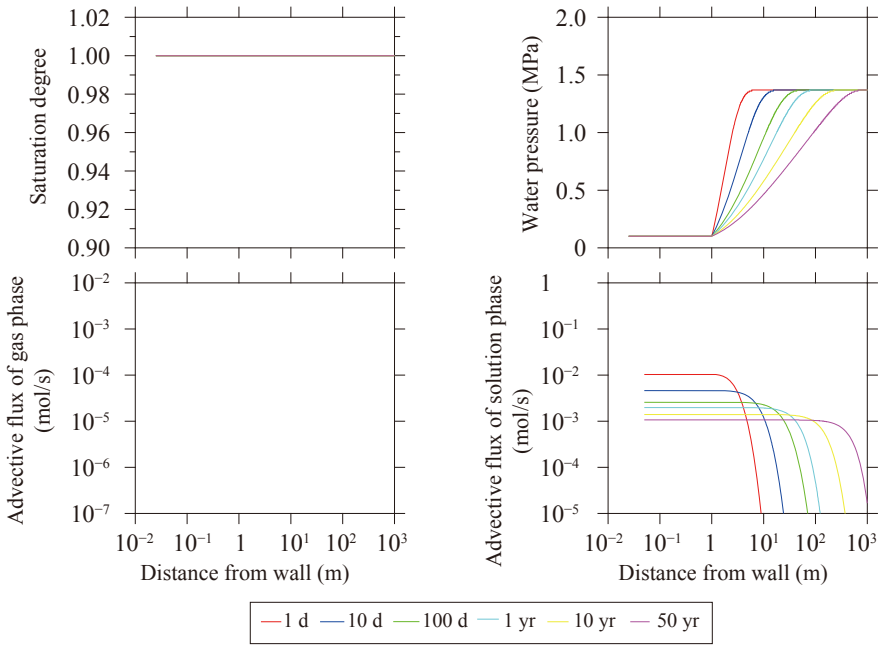

Fig. 6 Simulation results for case 4

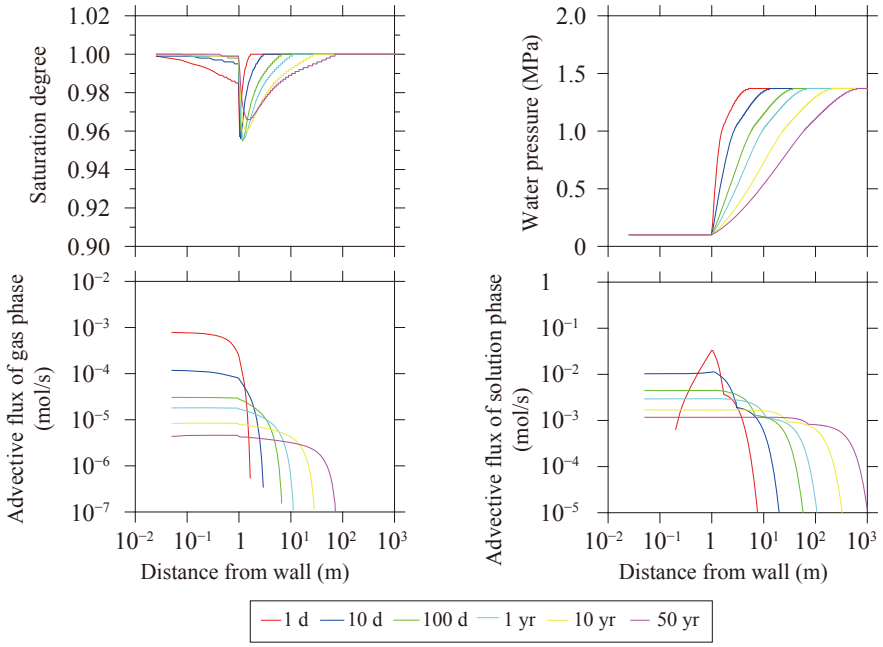

Fig. 7 Simulation results for case 5

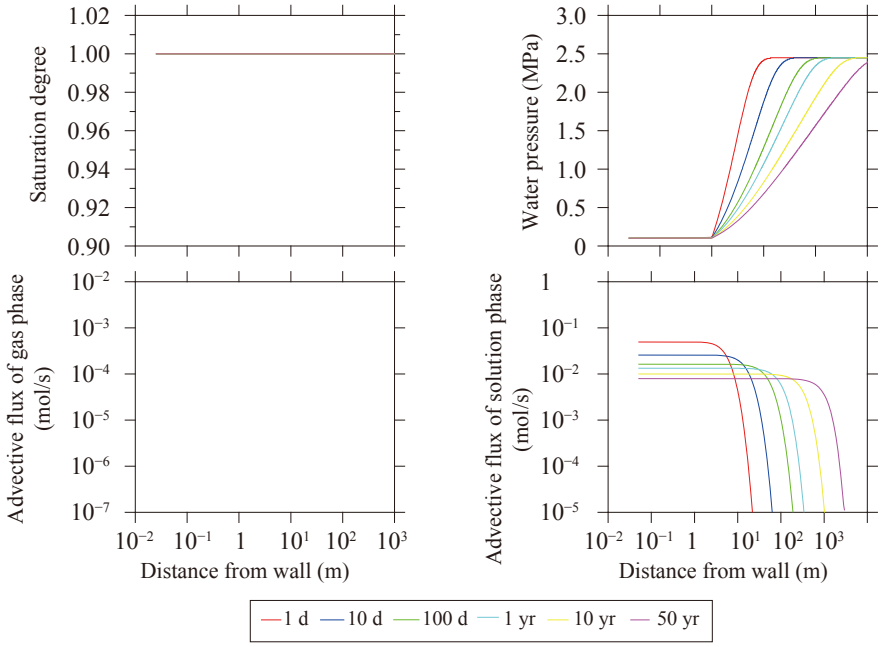

Fig. 8 Simulation results for case 6

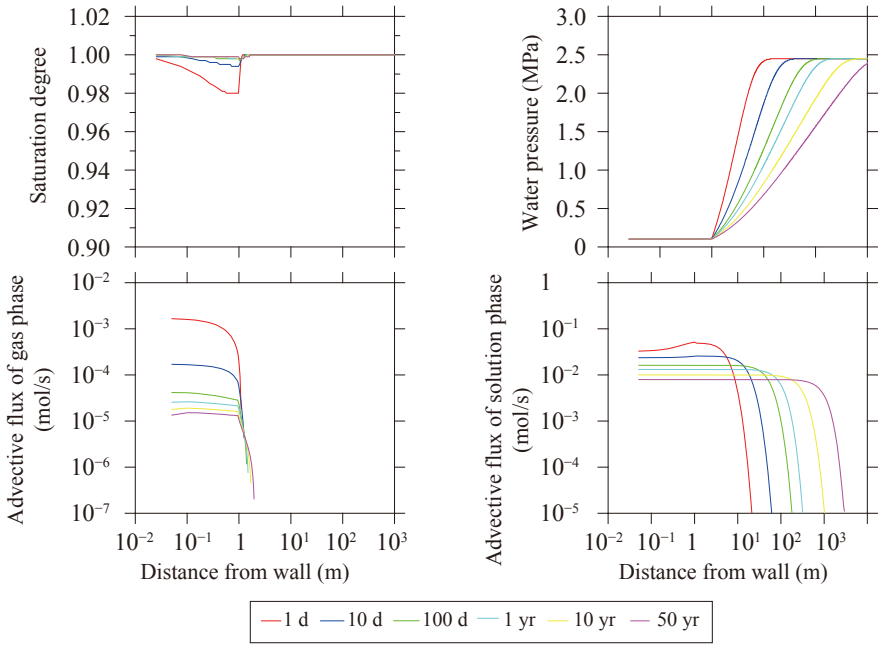

Fig. 9 Simulation results for case 7

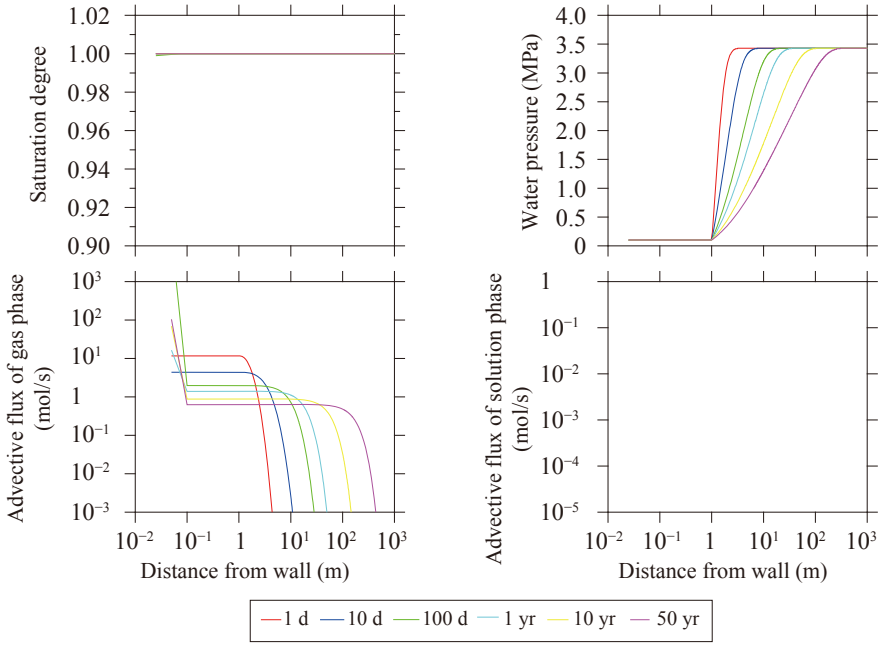

Fig. 10 Simulation results for case 8

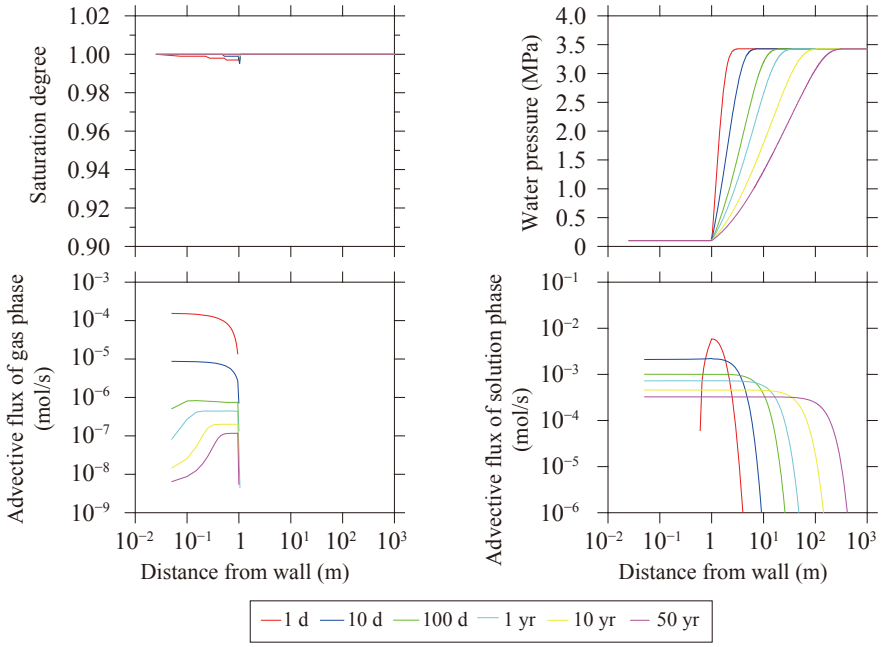

Fig. 11 Simulation results for case 9

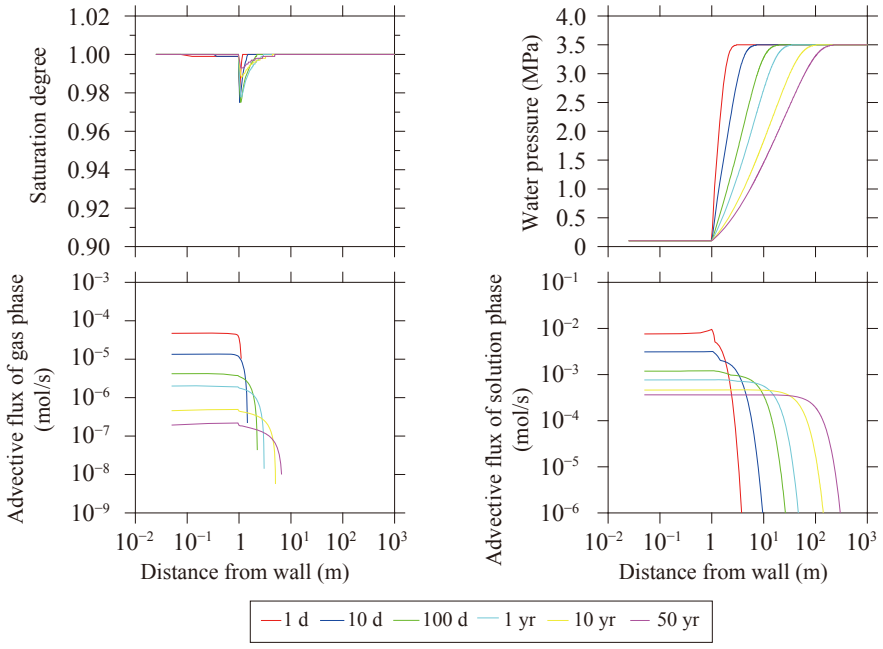

Fig. 12 Simulation results for case 10

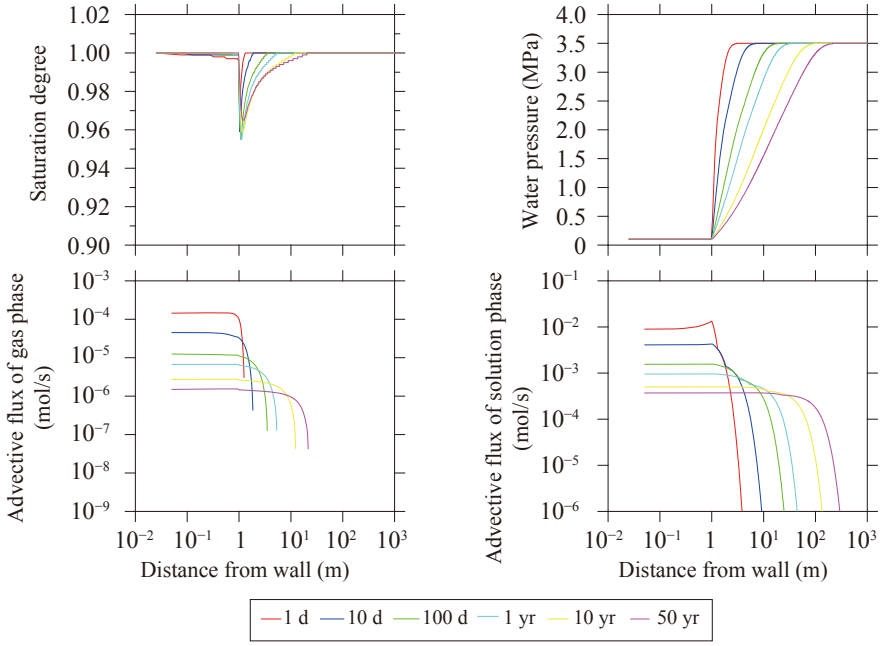

Fig. 13 Simulation results for case 11

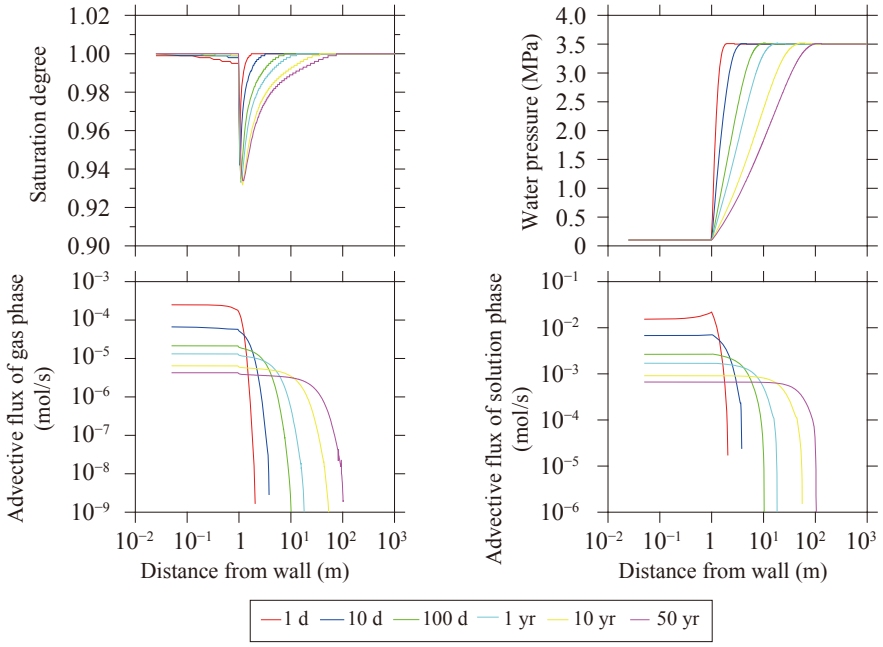

Fig. 14 Simulation results for case 12

3.2.2 Effect of rock permeability

Results for cases 13–18 are shown in Figs 15–20, respectively. Water pressure decreased with time in all cases, and drastically decreased in the EDZ within 1 day, except for cases 14 and 18. Miyakawa et al. (2019 and 2021)[10), 11)] discuss and describe in detail the desaturation and oxygen infusion.

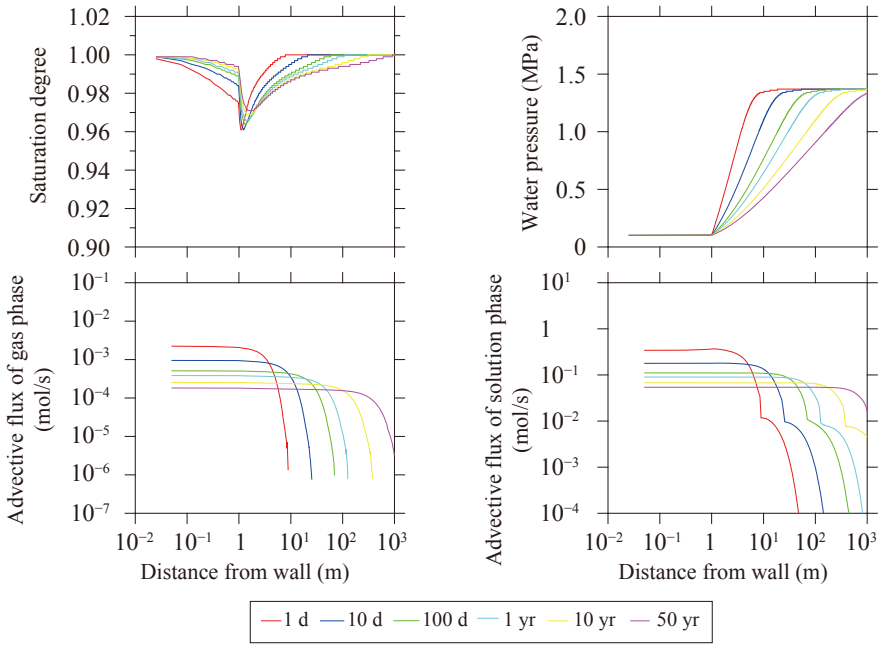

Fig. 15 Simulation results for case 13

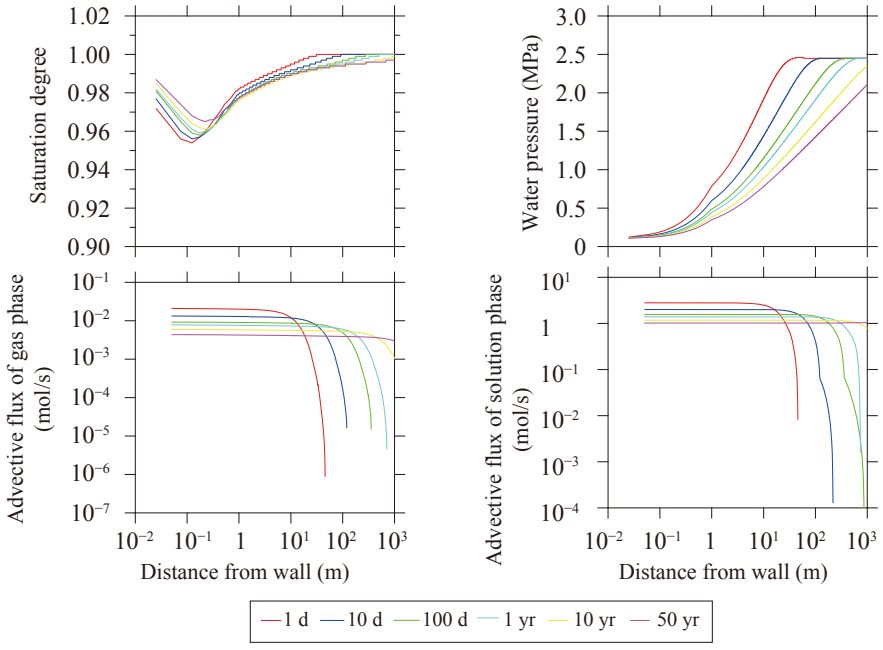

Fig. 16 Simulation results for case 14

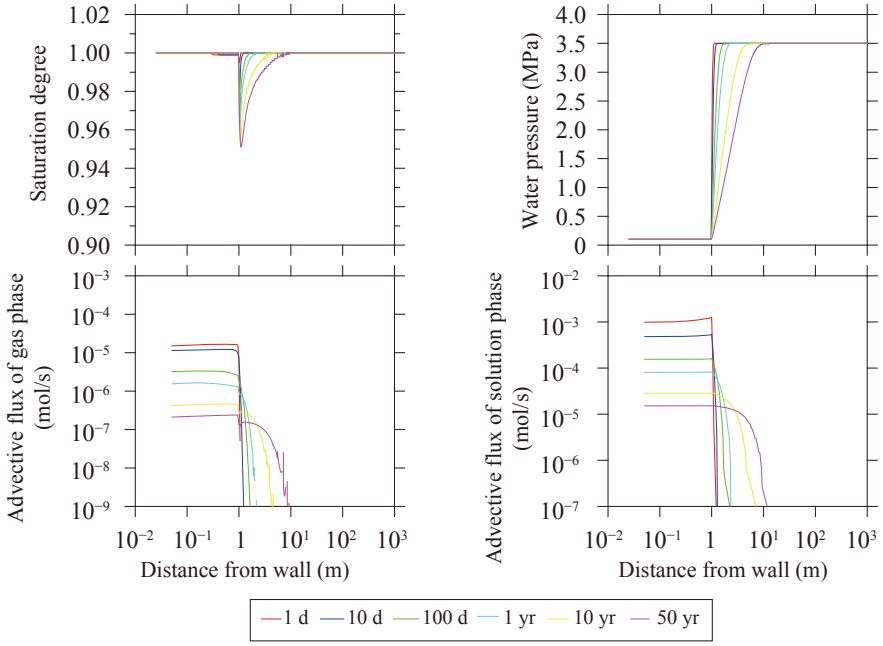

Fig. 17 Simulation results for case 15

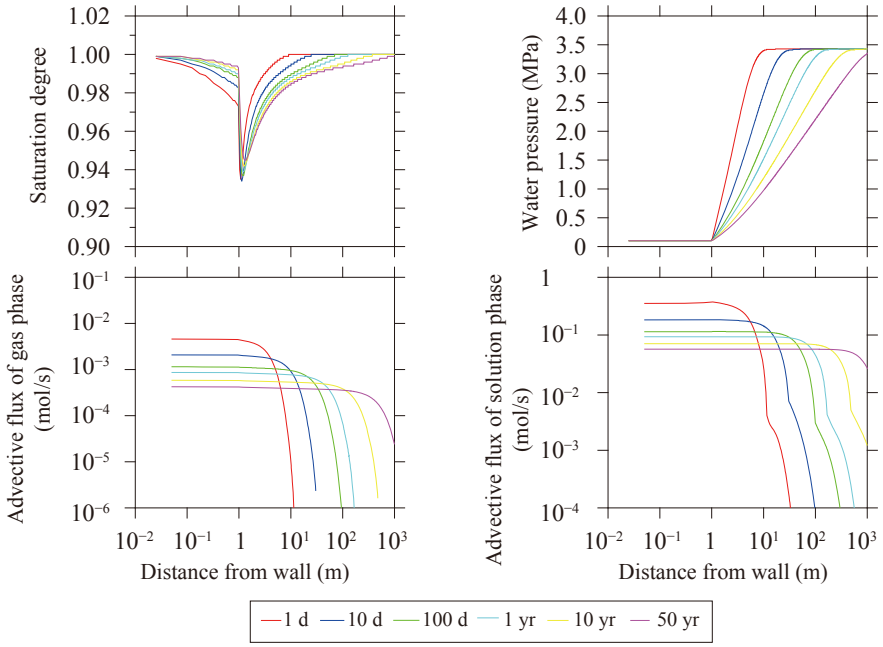

Fig. 18 Simulation results for case 16

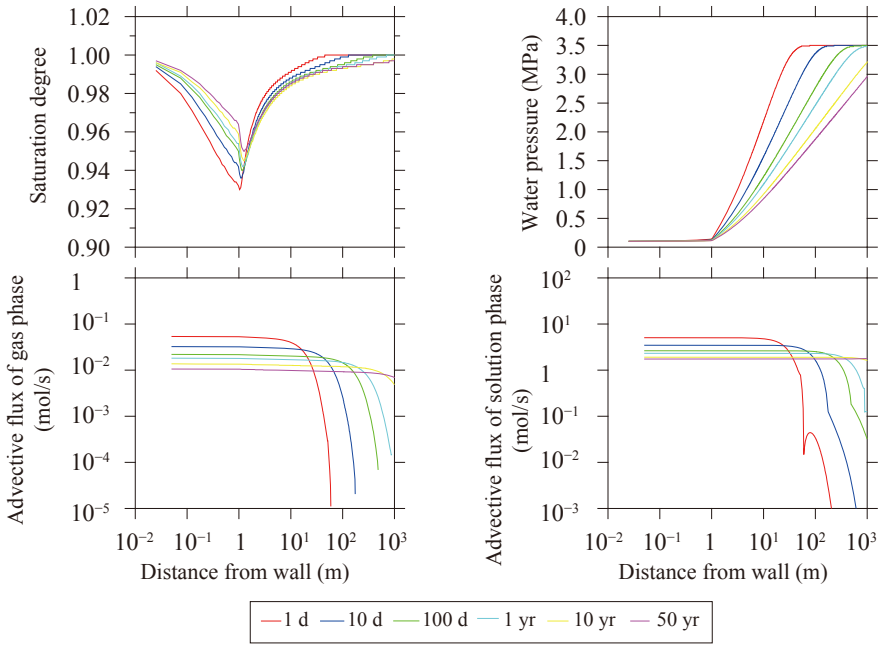

Fig. 19 Simulation results for case 17

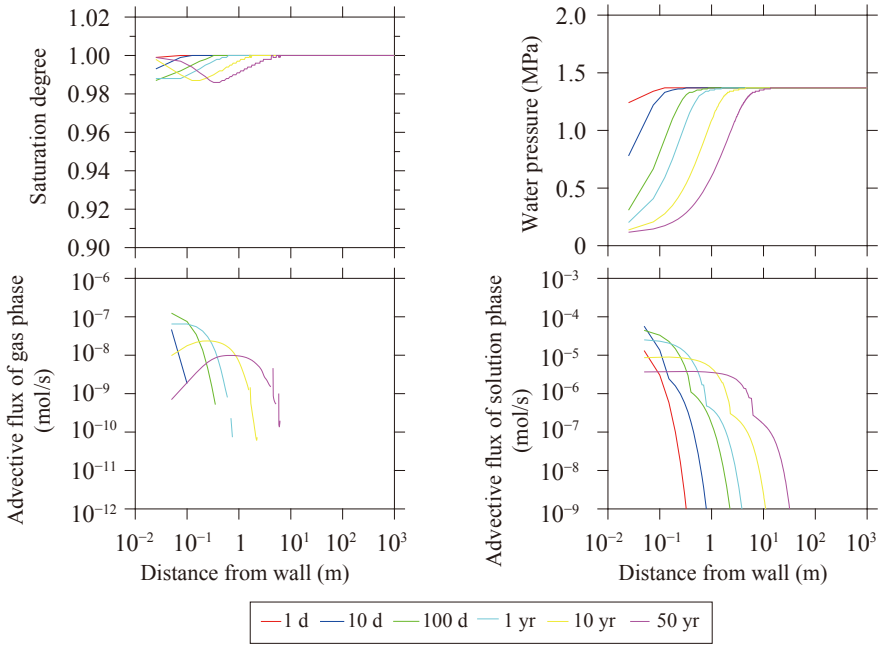

Fig. 20 Simulation results for case 18

3.2.3 Effect of humidity at the gallery wall

Results for cases 19–21 are shown in Figs 21–23, respectively. The saturation degree largely decreased, especially for cases 19 and 20, relative to cases with 100% humidity at the gallery wall. Water pressure decreased with time in all cases, and drastically decreased in the EDZ within 1 day. Miyakawa et al. (2021)[11] discuss and describe in detail the desaturation and oxygen infusion.

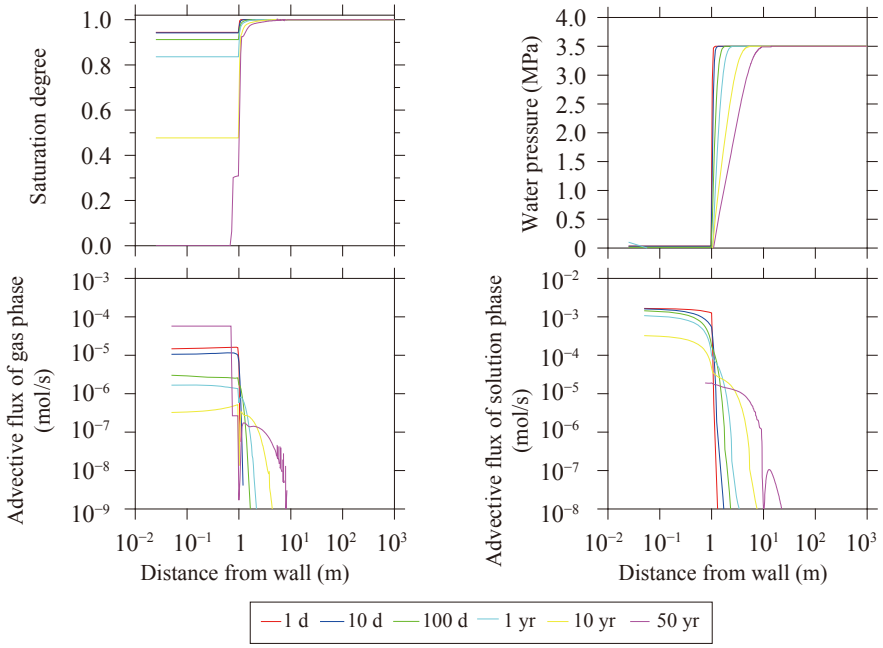

Fig. 21 Simulation results for case 19

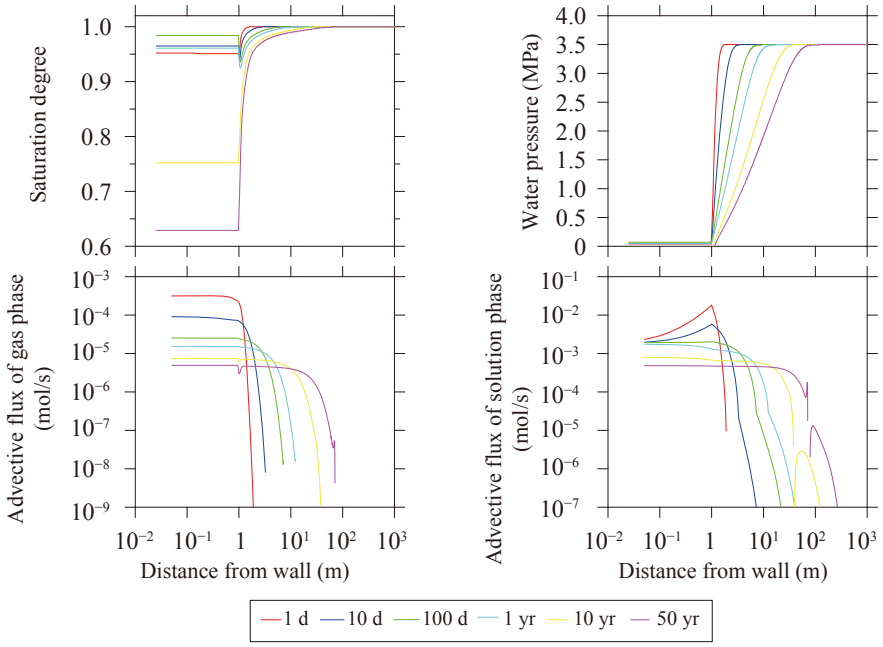

Fig. 22 Simulation results for case 20

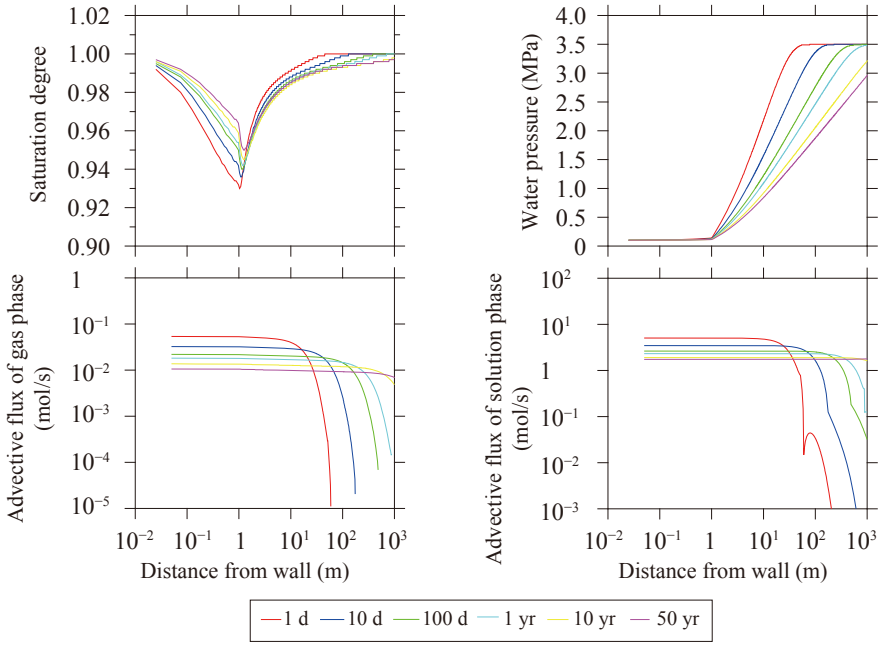

Fig. 23 Simulation results for case 21

3.2.4 Recovery from desaturation after drift backfilling

Results for cases 26–31 are shown in Figs 24–29, respectively. Case 26 (Fig. 24) had the saturation degree recover to almost full saturation after 100–500 years from backfilling. Water pressure also recovered to its initial condition of hydrostatic pressure in the same period. Case 27 (Fig. 25) had the saturation degree recover to full saturation after 10–100 years. Water pressure recovered to hydrostatic pressure after 100–500 years. Case 28 (Fig. 26) had the saturation degree recover within 1 year, although water pressure took 100–500 years to recover.

Case 29 (Fig. 27) had the saturation degree recover to full saturation after 1–10 years. Water pressure recovered to its initial condition after 10–100 years. Case 30 (Fig. 28) needed over 1000 years for full recovery of the saturation degree, and water pressure did not return to its initial condition even after 1000 years. Results for case 31 (Fig. 29) were similar to those of base case 26.

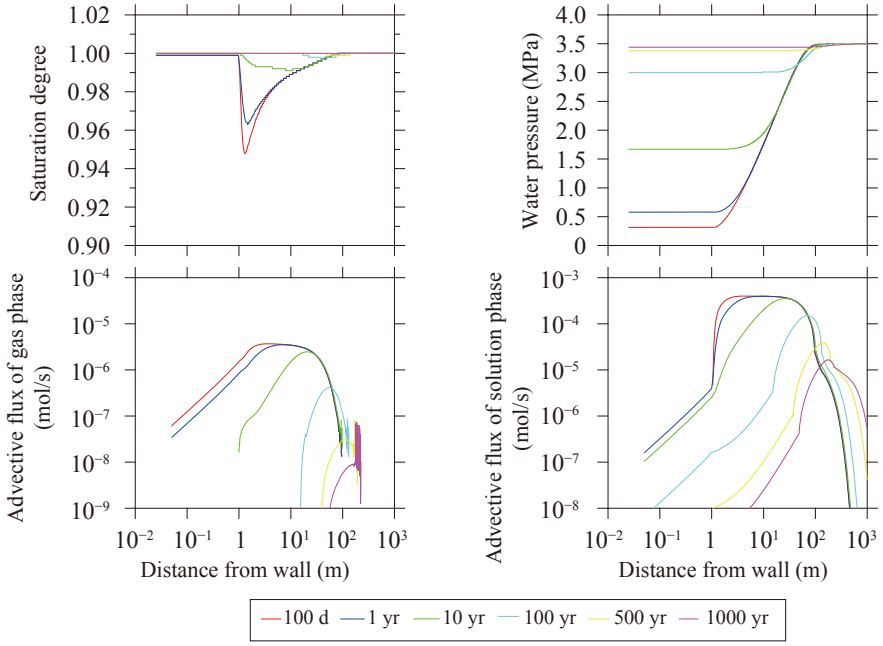

Fig. 24 Simulation results for case 26

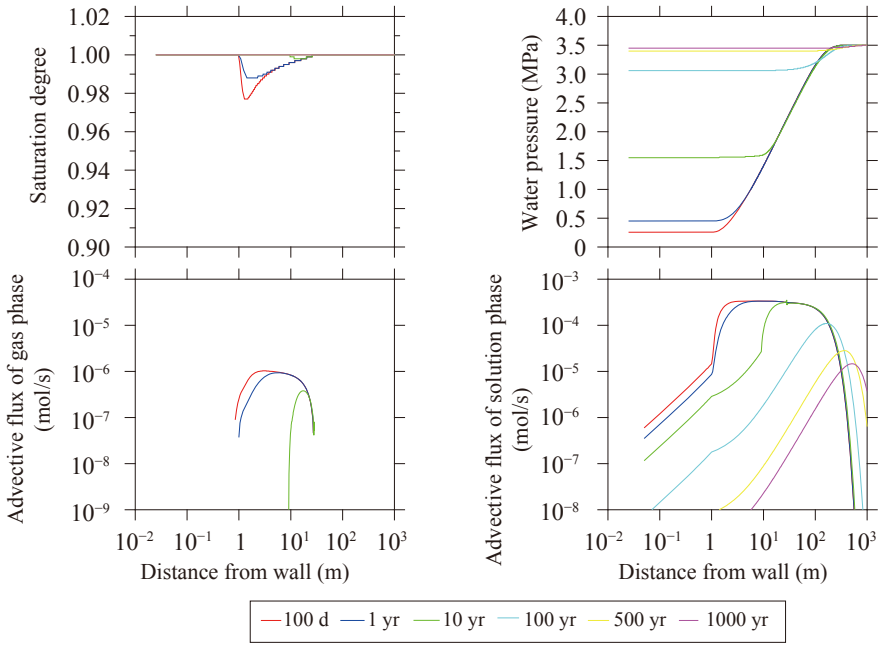

Fig. 25 Simulation results for case 27

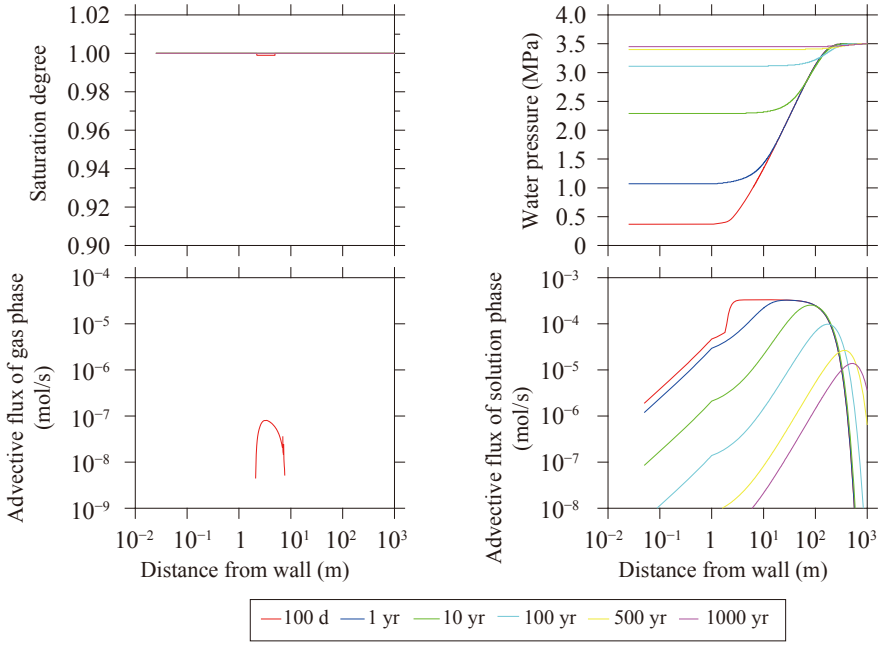

Fig. 26 Simulation results for case 28

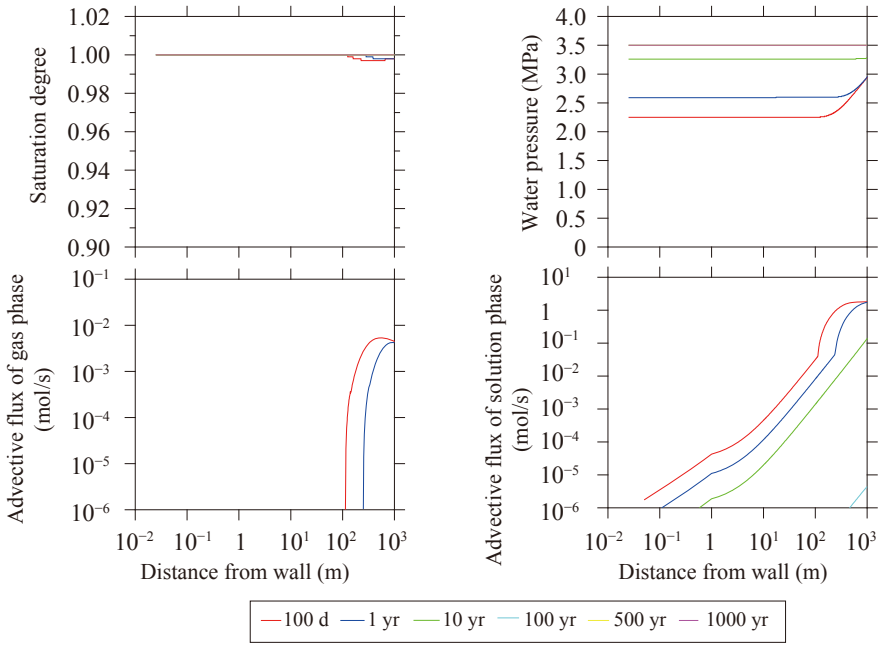

Fig. 27 Simulation results for case 29

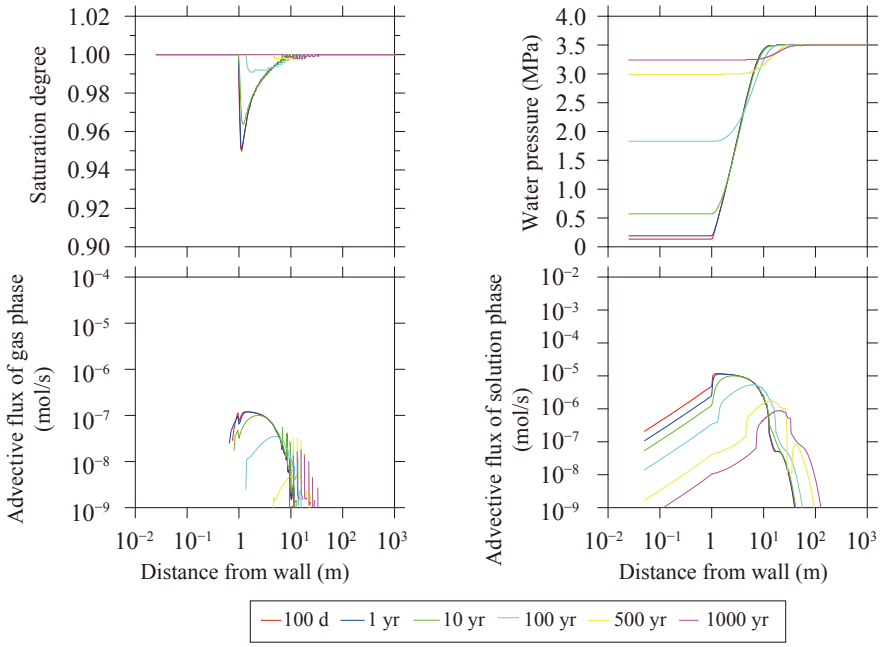

Fig. 28 Simulation results for case 30

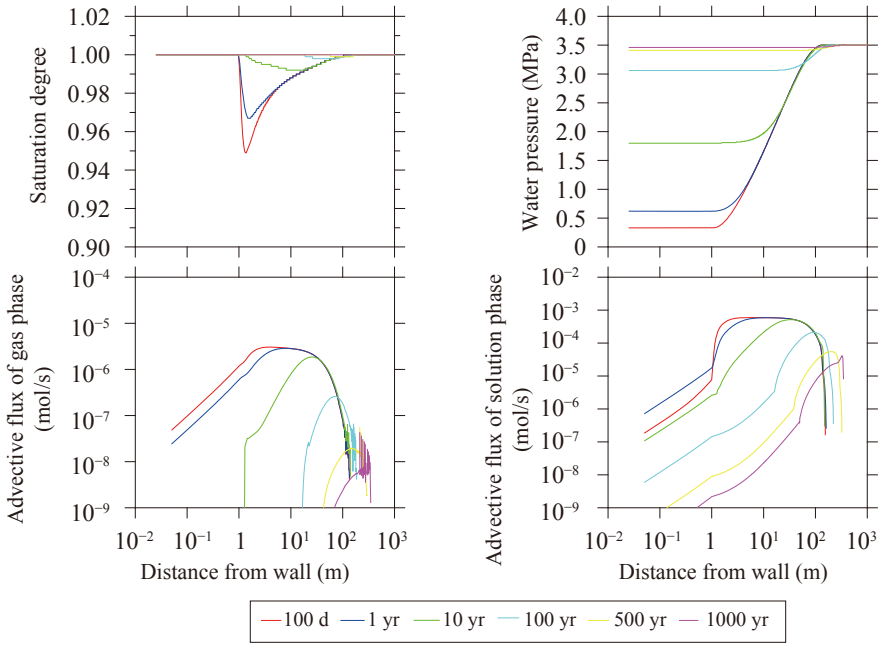

Fig. 29 Simulation results for case 31

3.2.5 Others

Results for cases 22–25 are shown in Figs 30–33, respectively. Water pressure decreased with time in all cases, and drastically decreased in the EDZ within 1 day. In all cases, the saturation degree dropped sharply to the fixed value of 60% at the boundary between the EDZ and the intact rock.

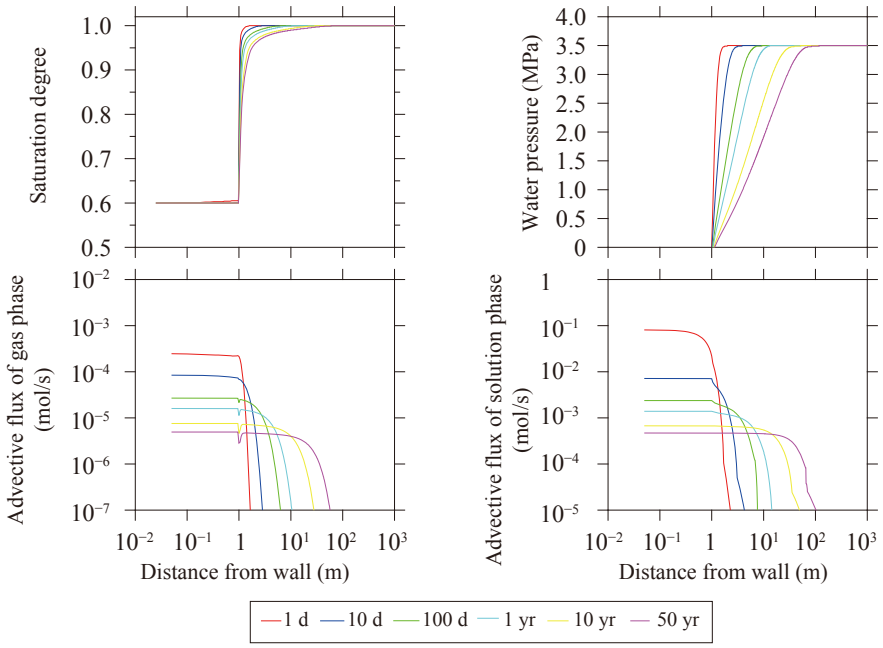

Fig. 30 Simulation results for case 22

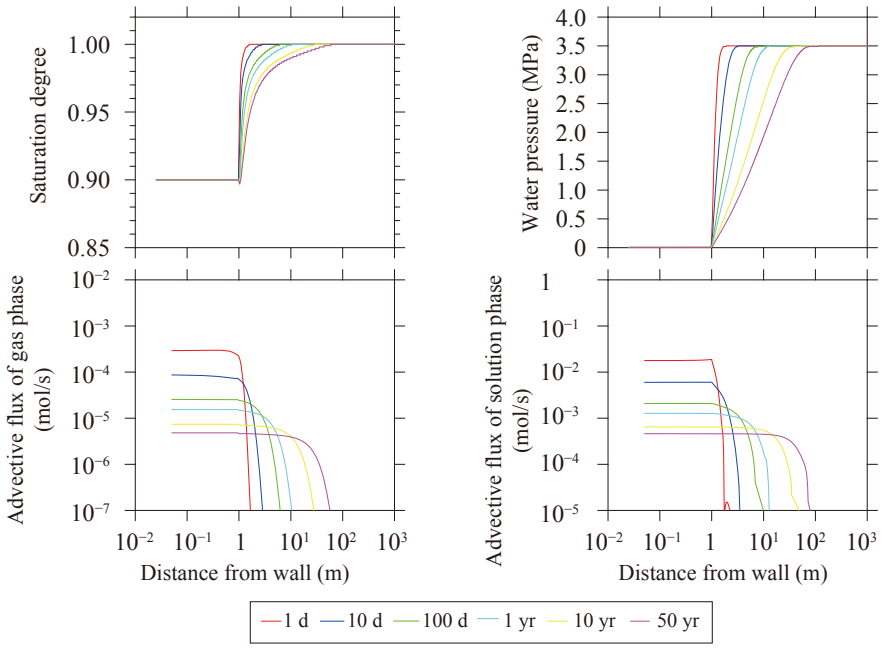

Fig. 31 Simulation results for case 23

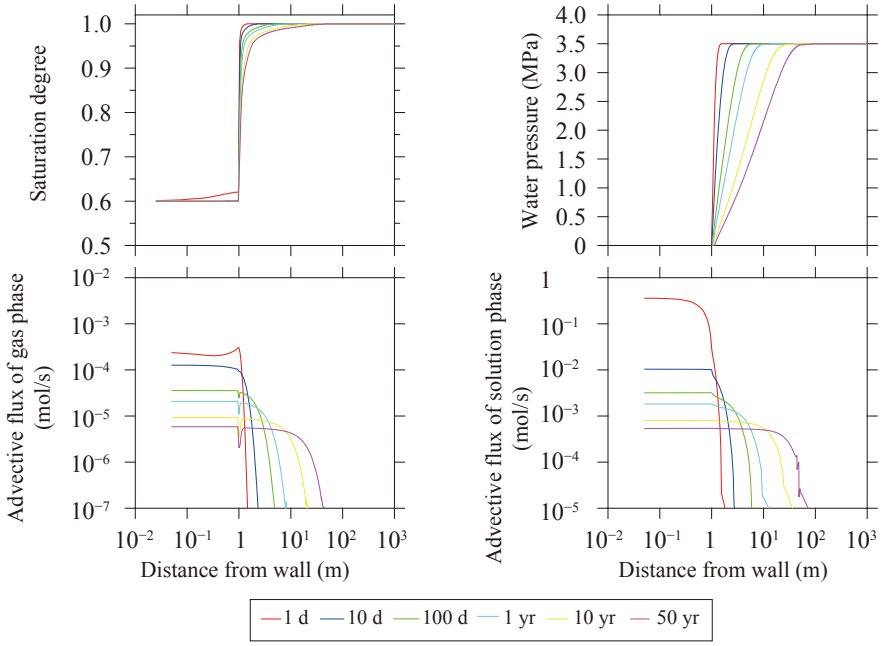

Fig. 32 Simulation results for case 24

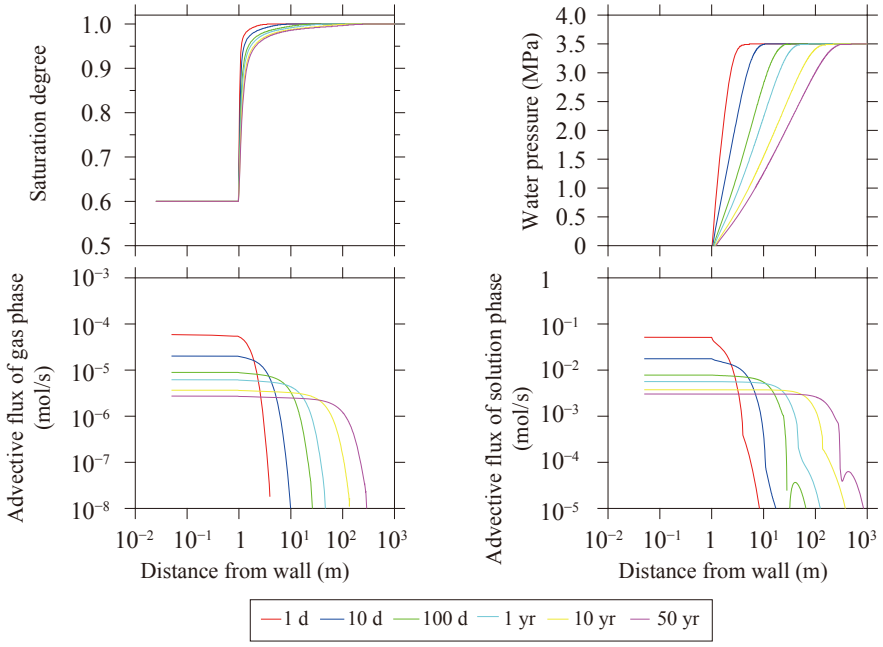

Fig. 33 Simulation results for case 25

4. Conclusion

In order to investigate the mechanisms of desaturation and oxygen infusion into sedimentary formations, Miyakawa et al. (2019 and 2021)[10), 11)] conducted numerical simulations. These investigations did not aim to completely reproduce and predict the exact behavior of fluid flow monitored in the HURL. This report presents all data for the output parameters, and includes data that

were not published in those studies to provide basic data for further developments. These simulations neglecting chemical reactions show an uppermost value of O_2 infusion. Chemical reactions related to O_2 buffering, such as pyrite oxidation (which consumes O_2), are potential mitigating factors. Precise predictions must consider the effects of such chemical reactions.

Nomenclature for data in Appendix

Time series for 27 output components are presented as text data in Microsoft Excel files. All data for each case are summarized in one file named *CaseXX.xlsx* where *XX* is the case number. Data at each time cross section are included as individual sheets named *initial*, *1 day*, *10 days*, *100 days*, etc.

Column A 'x (m)' is the distance from the gallery wall, and each value of the components in columns B–K corresponds to the distance in column A. Column B 'FLOH (J/s)' is the heat flow. Column C 'FLOGAS (mol/s)' is the flux of the gaseous phase. Column D 'FLOAQ (mol/s)' is the flux of the solution phase. Column E 'VELGAS (m/s)' is the flow velocity of the gaseous phase. Column F 'VELWAT (m/s)' is the flow velocity of the solution phase. Column G 'FDIFW (mol/s)' is the diffusive flux of the solution phase. Column H 'FDIFCH4 (mol/s)' is the diffusive flux of CH_4. Column I 'FDIFCO2 (mol/s)' is the diffusive flux of CO_2. Column J 'FDIFO2 (mol/s)' is the diffusive flux of O_2. Column K 'FDIFN2 (mol/s)' is the diffusive flux of N_2.

Column M 'X (m)' is the distance from the gallery wall, and each value in columns N–AD refers to this distance. Column N 'P (Pa)' is the pressure of the gaseous phase. Column O 'T (K)' is temperature. Column P 'SG' is the degree of desaturation. Column Q 'SW' is the degree of saturation. Column R 'PCWG (Pa)' is the capillary pressure. Column S 'DGAS (kg/m^3)' is the density of the gaseous phase. Column T 'PW (Pa)' is the pressure of the solution phase. Column U 'XWATG' is the molar ratio of water in the gaseous phase. Column V 'XCH4G' is the molar ratio of CH_4 in the gaseous phase. Column W 'XCO2G' is the molar ratio of CO_2 in the gaseous phase. Column X 'XO2G' is the molar ratio of O_2 in the gaseous phase. Column Y 'XN2G' is the molar ratio of N_2 in the gaseous phase. Column Z 'XWATL' is the molar ratio of water in the solution phase. Column AA 'XCH4L' is the molar ratio of CH_4 in the solution phase. Column AB 'XCO2L' is the molar ratio of CO_2 in the solution phase. Column AC 'XO2L' is the molar ratio of O_2 in the solution phase. Column AD 'XN2L' is the molar ratio of N_2 in the solution phase.

Acknowledgement

The authors thank Stallard Scientific Editing for proofreading English in the manuscript.

References

1) Matray, J.M., Savoye, S., Cabrera, J., Desaturation and structure relationships around drifts excavated in the well-compacted Tournemire's argillite (Aveyron, France), Eng. Geol., vol. 90, 2007, pp. 1–16.
2) Tsang, C.F., Bernier, F., Davies, C., Geohydromechanical processes in the Excavation Damaged Zone in crystalline rock, rock salt, and indurated and plastic clays–in the contest of radioactive waste disposal, Int. J. Rock Mech. Min. Sci., vol. 42, 2005, pp. 109–125.
3) Mazurek, M., Pearson, F.J., Volckaert, G., Bock, H., Features, Events and Processes Evaluation Catalogue for Argillaceous Media, Radioactive Waste Management, OECD/NEA, ISBN 93-64-02148-5, 2003, p. 376.
4) Mäder, U., Mazurek, M., Oxidation phenomena and processes in Opalinus Clay: Evidence from the excavation disturbed zones in Hauenstein and Mt. Terri tunnels, and Siblingen open clay pit, Materials Res. Soc. Symp. Proc., vol. 506, 1998, pp. 731–739.
5) De Craen, M., Van Geet, M., Honty, M., Weetjens, E., Sillen, X., Extent of oxidation in Boom Clay as a result of excavation and ventilation of the HADES URF: Experimental and modelling assessments, Phys. Chem. Earth, vol. 33, 2008, pp. S350–S362.
6) Oyama, T., Kubota, K., Weathring on unlined tunnel walls at sedimentary soft rocks after excavation – Investigation at Horonobe URL -, Proc. JSEG Ann. Meet., 2018, pp. 13–14 (in Japanese).
7) Miyakawa, K., Ishii, E., Hirota, A., Komatsu, D.D., Ikeya, K., Tsunogai, U., The role of low-temperature organic matter diagenesis in carbonate precipitation within a marine deposit, Appl. Geochem., vol. 76, 2017, pp. 218–231.
8) Nago, M., Motoshima, T., Miyakawa, K., Kanie, S., Sanoki, S., Three-dimensional visualization of methane concentration distribution in tunnels to increase underground safety, Proc. World Tunnel Cong. 2017, 2017, 10p.
9) Mochizuki, A., Ishii, E., Miyakawa, K., Sasamoto, H., Mudstone redox conditions at the Horonobe Underground Research Laboratory, Hokkaido, Japan: Effects of drift excavation, Eng. Geol., vol. 267, 2020, 105496.
10) Miyakawa, K., Aoyagi, K., Sasamoto, H., Akaki, T., Yamamoto, H., The effect of dissolved gas on rock desaturation in artificial openings in geological formations, Extended abstract of YSRM2019 and REIF2019, Ginowan, Japan, 2019, 6p.
11) Miyakawa, K., Aoyagi, K., Akaki, T., Yamamoto, H., Numerical simulation of oxygen infusion into desaturation resulting from artificial openings in sedimentary formations, 15th Japan Symposium on Rock Mechanics, Osaka, Japan, 2021, 6p.
12) Miyakawa, K., Okumura, F., Improvements in drill-core headspace gas analysis for samples from microbially active depths, Geofluids, vol. 2018, 2018, Article ID 2436814.
13) Pruess, K., Battistelli, A., TMVOC, a numerical simulator for three-phase non-isothermal flows of multicomponent hydrocarbon mixtures in saturated-unsaturated heterogeneous media, LBNL–

49375, Lawrence Berkeley National Lab., Berkeley, CA, 2002.

14) Jung, Y., Pau, G.S.H., Finsterle, S., Doughty, C., TOUGH3 User's Guide Version 1.0, LBNL–2001093, Lawrence Berkeley National Laboratory, Berkeley, CA, 2018, 163p.

15) Verma, A., Pruess, K., Thermohydrological conditions and silica redistribution near high-level radioactive waste emplaced in saturated geological formations, J. Geophys. Res., vol. 93, 1988, pp. 1159–1173.

16) Van Genuchten, M.TH., A closed-form equation for predicting the hydraulic conductivity of unsaturated soils, Soil Sci. Soc. Am. J., vol. 44, 1980, pp. 892–898.

17) Yamamoto, H., Shimo, M., Kunimaru, T., Kurikami, H., Preliminary simulation of degassing of natural gases dissolved in groundwater during shaft excavation in Horonobe underground research project, Proc. 36th Symp. Rock Mech., 2007, pp. 293–298 (in Japanese with English abstract).

18) Sugita, Y., Aoyagi, K., Kubota, K., Nakata, E., Ohyama, T., A study of the evaluation of the excavation damaged zone in the Horonobe underground research laboratory, 1 -Investigation in the 140 m gallery- (Joint research), JAEA-Research 2018-002, Japan Atomic Energy Agency, 2018, 72p. (in Japanese with English abstract).

19) Kurikami, H., Takeuchi, R., Yabuuchi, S., Scale effect and heterogeneity of hydraulic conductivity of sedimentary rocks at Horonobe URL site, Phys. Chem. Earth, vol. 33, 2008, pp. S37–S44.

20) Aoyagi, K., Kubota, K., Nakata, E., Suenaga, H., Nohara, S., A study of the evaluation of the excavation damaged zone in the Horonobe underground research laboratory, 2-Investigation in the 250 m gallery- (Joint research), JAEA-Research 2017-004, Japan Atomic Energy Agency, 2017, 91p. (in Japanese with English abstract).

21) Yoshino, H., Samata, Y., Niunoya, S., Ishii, E., Hydraulic tests for the excavation damaged zone around the 350 m niches in the Horonobe underground research project, JAEA-Data/Code 2018-015, Japan Atomic Energy Agency, 2019, 169p. (in Japanese with English abstract).

22) Aoyagi, K., Ishii, E., A method for estimating the highest potential hydraulic conductivity in the excavation damaged zone in mudstone, Rock Mech. Rock Eng., vol. 52, 2019, pp. 385–401.

23) Ota, K., Abe, H., Kunimaru T., eds., Horonobe underground research laboratory project synthesis of phase I investigation 2001–2005 volume "Geoscientific research", JAEA-Research 2010-068, Japan Atomic Energy Agency, 2011, 370p.

24) Tamamura, S., Miyakawa, K., Aramaki, N., Igarashi, T., Kaneko, K., A proposed method to estimate in situ dissolved gas concentrations in gas-saturated groundwater, Groundwater, vol. 56, 2018, pp. 118–130.